J Mater Sci: Mater Electron (2017) 28:15861–15869
DOI 10.1007/s10854-017-7480-7

Sonication-assisted deposition–precipitation synthesis of graphitic C_3N_4/BiOCl heterostructured photocatalysts with enhanced rhodamine B photodegradation activity

Lingjun Song[1] · Yanjun Zheng[1] · Changfeng Chen[1]

Received: 9 May 2017 / Accepted: 3 July 2017 / Published online: 25 July 2017

Abstract Novel two-dimensional graphitic carbon nitride (g-C_3N_4)/BiOCl nanosheets with excellent photodegradation activity towards rhodamine B (RhB) under visible light irradiation have been successfully synthesized by a sonication-assisted deposition–precipitation route. The composite nanosheets exhibited good dispersity and abundant contact interfaces, which led to the formation of *p–n* heterojunctions. Hybridization of g-C_3N_4 in the composites resulted in an extended absorption range and inhibited the recombination of the photoinduced charge carriers. Therefore, the two-dimensional heterostructure of the present compounds contributed to enhance their photocatalytic performances. In addition, the indirect photosensitization effect of RhB also influenced the photodegradation activity of BiOCl.

1 Introduction

Semiconductor photocatalysi is onsidered as a promising "green" oute to address environmental issues and the energy crisis [1, 2]. Recently, Bi(III)-based semiconductors such as $BiPO_4$ [3], $(BiO)_2CO_3$ [4, 5], $Bi_{12}TiO_{20}$ [6], Bi_2WO_6 [7, 8], $BiFeO_3$ [9, 10], Bi_2MoO_6 [11], $BiNbO_6$ [12], and $BiVO_4$ [13, 14], $(BiO)_2CO_3$ [15, 16], etc. have attracted significant interest for their potential application in photocatalytic degradation, photoanodes, water splitting, and electronic miniature devices. However, most of these photocatalysts are still affected by limited light absorption and inefficient separation of photogenerated carriers, which restrict their practical applications [17]. These issues highlight the importance of investigating novel visible-light-driven or other hybrid photocatalysts with low electron–hole recombination rate. Photocatalysts that respond to visible light irradiation represent promising materials for efficient solar light conversion [18]. Moreover, heterostructured photocatalysts offer additional advantages in terms of light absorption and charge separation [19]. Among Bi(III)-based semiconductors, bismuth oxyhalides (BiOX, X = Cl, Br, I) are important V–VI–VII ternary semiconductors with an indirect-transition band gap and a layered structure. BiOCl is a wide band gap semiconductor, which tends to form two-dimensional (2D) structures; however, its photocatalytic applications are limited, because it only responds to UV light and its efficiency in separating photoinduced electron–hole pairs is low. In order to address these issues, it is important to explore modifications of BiOCl capable of expanding its light response range and improving its efficiency in separating the photogenerated charge carriers. To date, several BiOCl-based compounds, including heterostructured $BiPO_4$/BiOCl [20], In_2O_3/BiOCl [21], Cu_2O/BiOCl [22], and Co_3O_4–loaded BiOCl nanoplates [23] and hollow Ag/AgCl/BiOCl microspheres [24], etc. have been considered as potential candidates for photocatalytic applications. These previous studies show that the presence of a heterostructure promotes photoinduced charge separation and enhances the photocatalytic properties of BiOCl-based semiconductor composites.

Coupling a *p*-type BiOCl semiconductor with the graphitic C_3N_4 (g-C_3N_4, an *n*-type semiconductor) is considered a suitable strategy to enhance the visible light

Electronic supplementary material The online version of this article (doi:10.1007/s10854-017-7480-7) contains supplementary material, which is available to authorized users.

✉ Yanjun Zheng
yanjun_zheng@hotmail.com

[1] Department of Materials Science and Engineering, College of Science, China University of Petroleum (Beijing), No. 18 Fuxue Rd., Beijing 102249, People's Republic of China

absorption of BiOCl and thus its potential photocatalytic applications. In this work, we fabricated *p–n* type heterostructured g-C_3N_4/BiOCl nanosheets with excellent photocatalytic activity towards the degradation of rhodamine B (RhB) under visible light irradiation. Compared with previous studies [25–27], the main findings of the present work are the highly dispersed composite nanosheets prepared here benefit from mild synthetic conditions and the presence of extended contact interfaces which promote the formation of *p–n* heterojunctions. While in Yang's work [28], g-C_3N_4/BiOCl hybrids, synthesized by ultrasonic method, with excellent photocatalytic activities in degrading methylene blue displayed nanoflake-shape with a thickness of above 200 nm and the obtained g-C_3N_4 exhibited block morphology. It is believable that the decrease in the thickness of the two-dimensional particles and the increase of the tight interface area between the two two-dimensional structures should contribute to the improvement of the catalytic performance in our research. Moreover, the high dispersity of the hybrid nanosheets is believed to be beneficial for adsorbing the RhB molecule on the surface of the catalysts and for absorbing the irradiated light. In addition, the 2D heterostructure contributes to improving the electron–hole transmission efficiency, ultimately enhancing the catalytic activity. A feasible mechanism for the photocatalytic activity of the 2D g-C_3N_4/BiOCl heterostructure is also discussed in detail.

2 Experimental details

All chemicals were of analytical grade and were used as received, without purification. Deionized (DI) water was employed throughout the experiments.

2.1 Preparation of ultrathin g-C_3N_4 nanosheets

Ultrathin g-C_3N_4 nanosheets were prepared according to a previous reported thermal polymerization approach [29]. In a typical procedure, 2 g of melamine and 4 g of ammonium chloride were thoroughly mixed together in a beaker, and then an appropriate amount of DI water was added. The mixture was then transferred to a muffle furnace and heated at 550 °C for 4 h, using NH_4Cl as a blowing agent in order to gain loose C_3N_4 production. The obtained g-C_3N_4 powders were ultrasonically exfoliated for 1 h. Finally, the suspension was centrifuged and washed with DI water and ethyl alcohol to remove impurities.

2.2 Synthesis of g-C_3N_4/BiOCl composites

The g-C_3N_4/BiOCl composite nanosheets were synthesized by sonication-assisted deposition–precipitation of BiOCl nuclei on the surface of protonated g-C_3N_4 nanosheets. The following synthetic procedure was employed: 0.004 mol of $Bi(NO_3)_3{\cdot}5H_2O$ and 0.004 mol of KCl were thoroughly dissolved in a solution consisted of 1.5 mL HCl and 5 mL DI water; then, a certain amount (0.05, 0.1, 0.2, 0.3, and 0.4 g) of g-C_3N_4 powders was added to the solution under continuous vigorous stirring for 1 h to allow sequential adsorption of Bi^{3+} and Cl^- ions on the surface of C_3N_4. In this process, aqueous HCl served not only for the dissolution of Bi^{3+} but also for the protonation of the g-C_3N_4 nanosheets. Afterward, the mixture was exposed to high-power ultrasound irradiation for 4 h while 25 mL of DI water was added dropwise. The DI water was added very slowly dropwise through an acid burette to ensure a normal evolution of the hydrolysis reaction of $Bi(NO_3)_3$ and avoid rapid nucleation of BiOCl on the rough surface of g-C_3N_4 or in the solution. After continuous stirring for another 1 h, the products were collected by centrifugation, washed several times with DI water to remove excess HCl, and dried in an oven at 60 °C for 12 h. The synthesized powders were then calcined at 300 °C for 1 h, which led to the final g-C_3N_4/BiOCl composites. The obtained samples are denoted as *x*CN/BiOCl, where *x* denotes the mass of g-C_3N_4.

For comparison, pure BiOCl was synthesized following the same procedure and experimental conditions, but without adding g-C_3N_4. Under continuous addition of DI water, the system changed from a transparent solution to a white suspension. Excess DI water was used to ensure the complete hydrolysis of Bi^{3+} to produce BiOCl. Pure BiOCl also can be denoted using the notation *x*CN/BiOCl introduced above, with the g-C_3N_4 mass *x* sets to zero.

2.3 Characterization of the photocatalysts

The crystal structure of the catalysts was characterized by X-ray diffraction (XRD) using a BrukerD8 Focus diffractometer operating with Cu Kα radiation, an accelerating voltage of 40 kV, and a current of 40 mA. The morphologies and microstructures of the composites were investigated by field-emission scanning electron microscopy (FESEM, Quanta 200F) with a 30 kV accelerating voltage and high-resolution transmission electron microscopy (HR-TEM, FEI TecnaiG2 F20) at 200 kV. The surface composition and chemical state of the elements present were determined by X-ray photoelectron spectroscopy (XPS, Thermo Fisher K-Alpha) with monochromatized Al Kα radiation in the 0–1200 eV range. The binding energies were calibrated with respect to the signal for adventitious carbon at 284.8 eV.

UV–Vis diffuse reflection spectra (DRS) were measured on a Shimadzu U-4100 spectrophotometer using $BaSO_4$ as a reference. The photoluminescence (PL) spectra of the photocatalysts were recorded by a Hitachi F-7000

fluorescence spectrometer using a Xe lamp with an excitation wavelength (λ_{ex}) of 370 nm at room temperature. Nitrogen adsorption–desorption isotherms were measured on a nitrogen adsorption apparatus (Micromeritics ASAP 2420) equipped with the micropore option system.

2.4 Evaluation of photocatalytic activity

The photocatalytic performances of the obtained products were evaluated by following the degradation of RhB under visible light irradiation at room temperature. A PLS-SXE 300W Xe arc lamp equipped with a UV-cutoff filter ($\lambda \geq$ 400 nm) was used as the light source. The light intensity employed was 35 mW/cm^2. In a typical photocatalytic experiment, 0.10 g photocatalysts were added to 100 mL of a 10 mg/L aqueous solution of RhB, without pH modulation, and the solution was magnetically stirred during the reaction. Before the photocatalytic experiment, the reaction vessel was stirred in the dark for 60 min to reach the absorption–desorption equilibrium of the dye on the catalyst surface, and the system was then exposed to the Xe lamp under magnetic stirring. Aliquots of about 4 mL of suspension were collected at intervals of 5 min during the photocatalytic process, centrifuged, and analyzed by a Shimadzu UV–Vis 1700 spectrophotometer with deionized water as a reference sample.

3 Results and discussion

3.1 Morphology and structure characterization

The morphology and microstructure of the *x*CN/BiOCl photocatalysts were inspected by SEM and TEM. As depicted in Fig. 1, the BiOCl nanosheets, with inhomogeneous crystallites smaller than 4 μm, display smooth surfaces

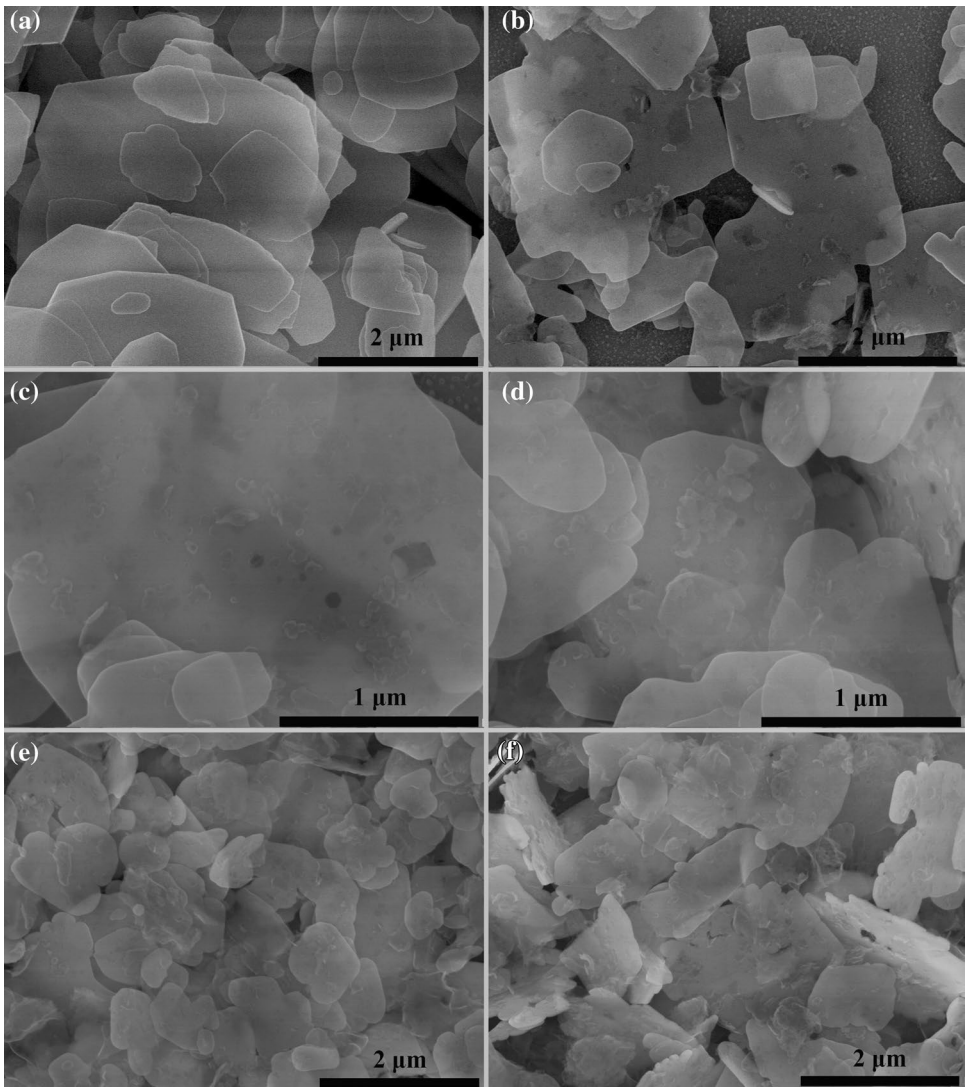

Fig. 1 SEM images of *x*CN/BiOCl composites with different g-C_3N_4 contents: **a** 0 g; **b** 0.05 g; **c** 0.1 g; **d** 0.2 g; **e** 0.3 g; **f** 0.4 g

and a thickness of less than 40 nm. Upon coupling with the g-C_3N_4 nanosheets, the surface of the BiOCl nanosheets becomes rougher and their thickness decreases to about 20 nm. The g-C_3N_4 fragments deposited on BiOCl can be easily identified. Figure 1f shows the cross section of the composite nanosheets and reveals that the ultrathin g-C_3N_4 nanosheets are irregularly stacked on both sides of the BiOCl nanosheets. Moreover, the SEM-mapping images (Fig. S1) of an individual composite nanosheet imply the distribution of Bi, V, O, C and N elements and demonstrate that g-C_3N_4 nanosheets are randomly dispersed on the surface of BiOCl. The mechanism leading to the formation of the heterostructure and to the generation of holes on the surface of composite nanosheets can be inferred by comparing the SEM images of pure BiOCl nanosheets and the composite nanosheets. First, HCl corroded the pristine, negatively-charged surface of g-C_3N_4, and Bi^{3+} might also be adsorbed on the same surface; chloride ions were then attracted around g-C_3N_4 by electrostatic interactions. As the hydrolysis of $Bi(NO_3)_3$ started, $[Bi_2O_2]^{2+}$ ions were formed and reacted with Cl^-, and large amounts of BiOCl nuclei were preferentially generated on the rough g-C_3N_4 surface in order to decrease the surface energy. BiOCl then grew into nanosheet crystals under continuous ultrasonic treatment, producing a unique 2D heterostructure. The nanosheets were extruded against one another. Finally, the ultrathin g-C_3N_4 nanosheets broke into smaller fragments, some of which were completely exfoliated from the BiOCl substrate, leaving some irregular holes on its surface. Figure 2 shows the TEM and HRTEM images of an individual 0.1CN/BiOCl composite nanosheet. Clear boundaries between ultrathin amorphous g-C_3N_4 and tetragonal BiOCl domains can be observed in the TEM images, with a lattice fringe of 0.27 nm corresponding to the (110) plane of tetragonal BiOCl. Furthermore, an obvious interface was observed between g-C_3N_4 and BiOCl, indicating the formation of a heterostructure.

3.2 Phase and surface composition analysis

Figure 3 shows the phase composition of the as-prepared samples. All diffraction peaks of the composites can be indexed to the tetragonal BiOCl phase (JCPDS No. 06-0249). A second phase, with a weak signal at 27.8°,

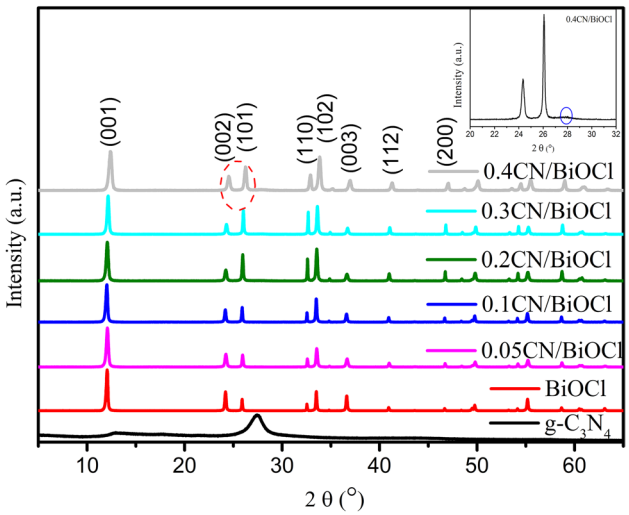

Fig. 3 XRD patterns of g-C_3N_4 and *x*CN/BiOCl composites with different C_3N_4 contents

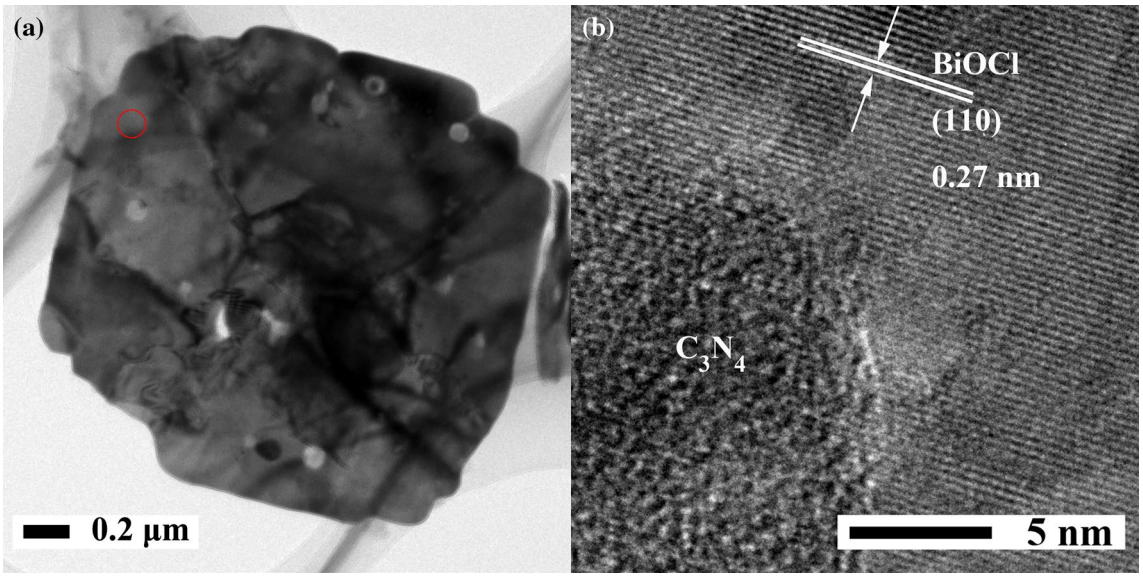

Fig. 2 TEM (**a**) and HRTEM (**b**) images of the 0.1CN/BiOCl heterostructured nanosheet

could be indexed to the (002) plane of g-C_3N_4 and was only observed in 0.4CN/BiOCl, indicating the low crystallinity of g-C_3N_4 in the composites. Compared with pure g-C_3N_4, the characteristic diffraction peak of the (002) plane is slightly shifted from 27.4° to larger angles, which might be attributed to the interaction between g-C_3N_4 and BiOCl. As the amount of g-C_3N_4 was increased, the average crystallite sizes of BiOCl (as calculated by the Debye–Scherrer equation) decreased from 36.8 nm (pure BiOCl) to 23.8 nm (0.4CN/BiOCl), in good agreement with the SEM results. At the same time, the (002)/(101) peak intensity ratio in *x*CN/BiOCl gradually changed, indicating that the main exposed BiOCl facets changed from {001} to {010} [27], bounded by 0.1CN/BiOCl. This result almost fits the conclusions reached by Zhang et al. [30] on the basis of the (002)/(200) peak intensity ratios.

XPS measurements were conducted to investigate the surface composition and chemical state of the different elements. As shown in Fig. 4, the 0.1CN/BiOCl photocatalysts consist of Bi, O, Cl, C, and N elements. The Bi 4f and Cl 2p high-resolution XPS spectra are shown in Fig. 4d, f, respectively. The characteristic Bi $4f_{7/2}$ and Bi $4f_{5/2}$ signals of the Bi^{3+} species [31] are found at 159.4 and 164.7 eV in 0.1CN/BiOCl, respectively, slightly shifted by 0.3 eV to lower binding energies compared to pure BiOCl. Similar blue shifts relative to pure BiOCl are displayed by the peaks at 198.1 and 199.7 eV in Fig. 4f, corresponding to the Cl $2p_{3/2}$ and Cl $2p_{1/2}$ orbitals of Cl^- in the composites. The shift of the Bi^{3+} and Cl^- binding energies in 0.1CN/BiOCl could be attributed to the strong electrostatic interaction between BiOCl and g-C_3N_4 [32]. The XPS peak at O 1*s* binding energy of 530.2 eV for both BiOCl and 0.1CN/BiOCl corresponds to Bi–O bonds in BiOCl, whereas the O 1*s* peak at 523.3 eV can be attributed to hydroxyl species or H_2O molecules absorbed on the surface of the photocatalysts [33]. The C 1*s* peak centered at about 284.8 eV in Fig. 4b can be ascribed to graphitic or adventitious carbon on the surface of g-C_3N_4 [34, 35], whereas the signal at 288.2 eV can be assigned to sp^2 C (N–C=N) in triazine rings [36, 37]. The N 1*s* XPS spectrum of the composite in Fig. 4c does not exhibit any apparent shift relative to BiOCl, except for the disappearance of the weak signal at 404.4 eV which is attributed to π-excitations [38, 39], revealing that BiOCl interacts with g-C_3N_4 via π-electrons [34] rather than C or N atoms. The maintained N1s signals are ascribed to sp^2-hybridized aromatic N (C=N–C), tertiary N (N–C_3) [40], and quaternary nitrogen [41] in the aromatic rings. The results of the present analysis thus confirm the coexistence of BiOCl and g-C_3N_4, and demonstrate the electrostatic interactions between BiOCl and the π-electrons in g-C_3N_4.

3.3 Optical properties and photocatalytic performance

Generally, the ability to harvest visible light is highly beneficial for the photocatalytic performance of a material.

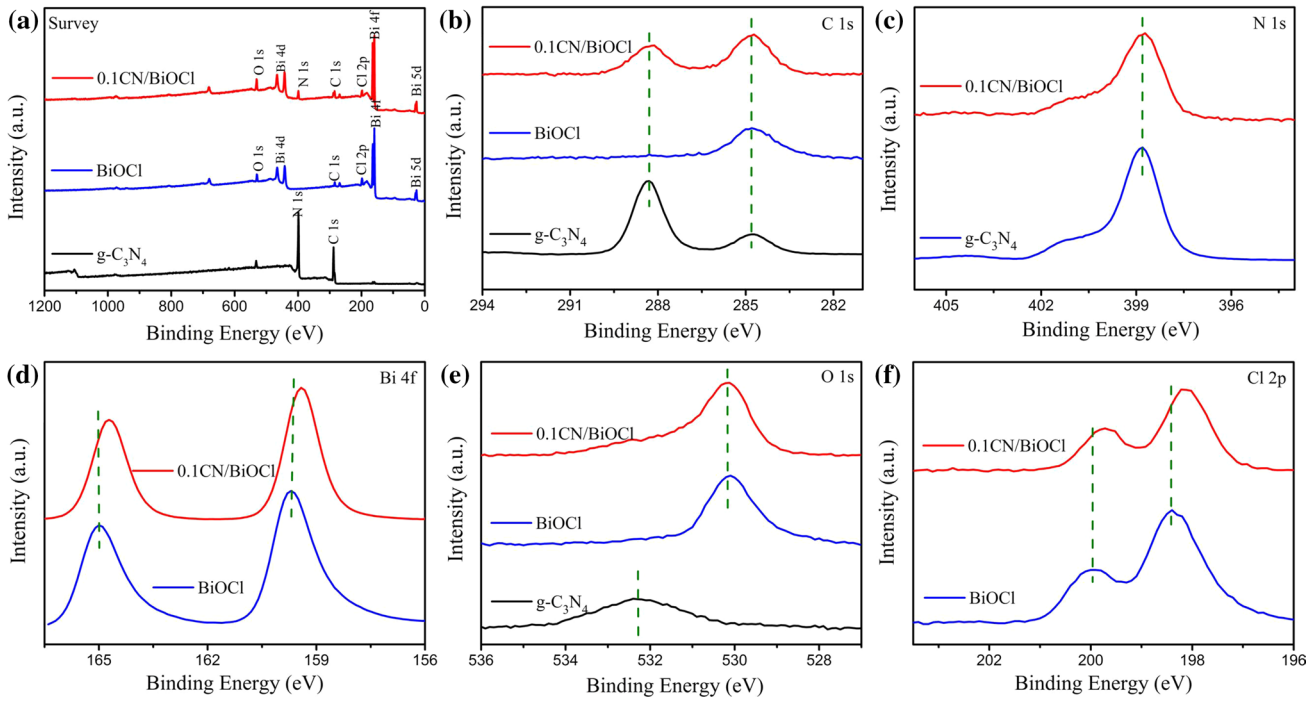

Fig. 4 XPS spectra of 0.1CN/BiOCl, g-C_3N_4, and BiOCl: **a** survey; **b** C1s; **c** N 1*s*; **d** Bi 4f; **e** O1*s*; **f** Cl 2p

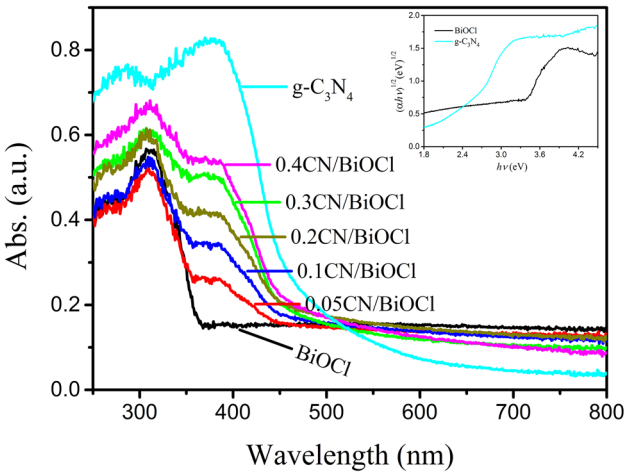

Fig. 5 UV–Vis DRS spectra of BiOCl, g-C_3N_4, and the *x*CN/BiOCl series; (*inserted*) Plots of $(\alpha h\nu)^{1/2}$ versus photon energy ($h\nu$) to obtain the band-gap energies of pure BiOCl and g-C_3N_4

Hence, we analyzed the optical absorption properties of the present composites. Figure 5 displays the typical UV–Vis diffuse reflectance spectra of all composites and the corresponding band gap energies of pure BiOCl and g-C_3N_4. Only UV light can be absorbed by pure BiOCl, while g-C_3N_4 responds to both UV and visible light. Upon combining BiOCl with g-C_3N_4, all composites showed good optical response properties. The spectra of the g-C_3N_4/BiOCl composites include both g-C_3N_4 and BiOCl absorption peaks at ~310 and ~380 nm, respectively, confirming the coexistence of the two individual components in the composites. The absorption bands of g-C_3N_4/BiOCl encompass slightly extended UV and visible light ranges compared with BiOCl, as a result of the hybridization. Moreover, the absorption intensities of the composite photocatalysts show a clear increase with raising g-C_3N_4 content, indicating an enhanced transfer of photoinduced electrons, which would contribute to improve the charge separation efficiency in the photochemical reactions. The corresponding band gap (E_g) values of the bare g-C_3N_4 and BiOCl, estimated by extrapolating the linear part of the Kubelka–Munk function, are 2.40 and 3.12 eV, respectively.

To better understand the band structure of the g-C_3N_4/BiOCl hybrids, the positions of the conduction band (CB) and valence band (VB) edges were calculated according to the Mulliken electronegativity theory, using the following empirical relation [42, 43]:

$$E_{VB} = \chi - E^e + 0.5E_g$$

where χ is the absolute electronegativity of the semiconductor ($c = 6.36$ and 4.73 eV for pure BiOCl and g-C_3N_4, respectively) and E^e is the energy of free electrons on the hydrogen scale (about 4.5 eV). The conduction band edge position can be calculated as $E_{CB} = E_{VB} - E_g$. Accordingly, the calculated E_{VB} and E_{CB} values were determined as +1.43 and −0.97 eV, respectively, for pure g-C_3N_4, and as +3.39 and +0.27 eV, respectively, for pure BiOCl. Therefore, well-matched staggered band structures are present in all g-C_3N_4/BiOCl *p–n* heterostructures, which is a favorable feature for effectively separating and thus suppressing the recombination of photoinduced charges.

The PL spectra of pure g-C_3N_4, BiOCl, and 0.1CN/BiOCl were measured to analyze the corresponding charge recombination rates in these systems. As shown in Fig. 6, the 0.1CN/BiOCl hybrids exhibit lower PL emission intensity than pure g-C_3N_4, indicating a lower recombination rate and a more efficient separation of the photoinduced charges in the heterojunction. However, BiOCl shows a weak PL emission peak around 415 nm, denoting a limited photogeneration of electron–hole pairs under visible light irradiation. The analysis of DRS and PL spectra suggests that the construction of heterostructure in photocalysts with staggered band structures effectively combines the beneficial properties of both semiconductors, resulting in a significantly improvement of both light absorption properties and charge separation efficiency.

To further evaluate the photocatalytic efficiency of the obtained photocatalysts, we assessed their activity in the photodegradation of RhB under visible light irradiation. For BiOCl, a wide band gap semiconductor, it should only have activity in ultraviolet light range. Conversely, as depicted in Fig. 7, the degradation rate of RhB over pure BiOCl nanosheets exposed {001} facets was up to 48.1% under visible light irradiation for 30 min, as a result of an indirect photosensitization mechanism rather than the

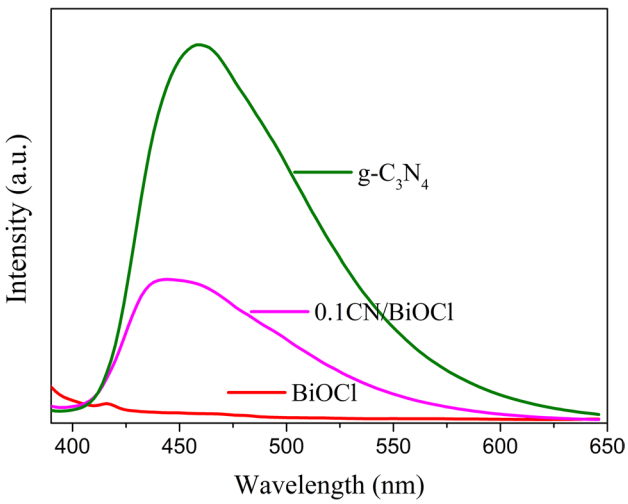

Fig. 6 PL spectra of pure g-C_3N_4, BiOCl, and 0.1CN/BiOCl composite photocatalysts ($\lambda_{ex} = 370$ nm)

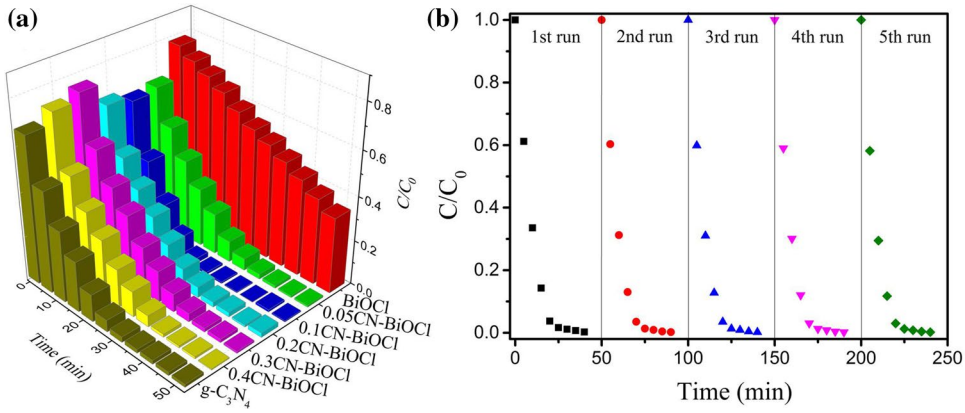

Fig. 7 **a** Photocatalytic efficiency in the degradation of RhB under visible light illumination (by a 300 W Xe arc lamp) over g-C_3N_4 and *x*CN/BiOCl composites with different contents of g-C_3N_4. **b** Assessment of the stability of the photocatalytic degradation activity of 0.1CN/BiOCl nanoflakes

direct band gap excitation doubtlessly, while it reached 98% for g-C_3N_4. It is also worth mentioning that the *x*CN/BiOCl series presented significantly enhanced photocatalytic properties compared with tetragonal BiOCl nanosheets, whose performances were extremely close to those of pure g-C_3N_4 nanosheets, effectively demonstrating the key role of the heterostructure in promoting the photocatalytic activity. The highest activity among all composites examined here was shown by the 0.1CN/BiOCl heterostructured nanosheets, exposing {010} facets of BiOCl. The activity of this composite was even higher than that of g-C_3N_4, indicating that an optimal g-C_3N_4/BiOCl ratio might produce efficient heterojunction interfaces between the two components and effectively hinder the recombination of charge carriers. However, the degradation rate of 0.3CN/BiOCl, exposing the {010} facets of BiOCl, was slight lower than that of 0.05CN/BiOCl, which exposed BiOCl {001} facets, demonstrating that the specific exposed facets of BiOCl might influence the migration of the charge carriers, but are not the main factor leading to the improved photocatalytic efficiencies of the composites. The decrease noted above may result from the nonuniform distribution of g-C_3N_4 or the agglomeration caused by the calcinations.

In addition, the stability of the heterostructure photocatalysts was investigated by reusing the 0.1CN/BiOCl sample in the degradation of RhB under visible light irradiation, repeated at 40 min intervals. As shown in Fig. 7b, almost no change in the photocatalytic activity of the sample was detected after five cycles, confirming the high stability of the 0.1CN/BiOCl composite and highlighting its potential for catalytic applications.

3.4 Mechanism of photocatalytic activity enhancement

To elucidate the nature of the active species in the photodegradation procedure, a series of trapping experiments were carried out individually which were similar to the photocatalytic process. 1,4-benzoquinone (BQ), isopropyl alcohol (IPA), and ethylenediamine tetraacetic acid disodium salt (EDTA-2Na) were adopted as superoxide radical ($\cdot O_2^-$), hydroxyl radical ($\cdot$OH), and hole (h^+) scavengers, respectively. The concentration of the trapping agents was fixed at 1 mM. As revealed in Fig. 8, the photodecomposition rate of RhB solution was hardly influenced by the addition of IPA, suggesting that ·OH groups have no significant oxidation effects, in good agreement with the calculated band energies. In the *p–n* heterostructure, the valence band of g-C_3N_4 was likely to provide the h^+ to oxidize the OH^- ions absorbed on the surface of the photocatalysts or the organic pollutant molecules. However, the valence band potential of excited g-C_3N_4 is 1.43 V, more negative than the redox potential of the $\cdot OH/OH^-$ pair (1.99 V vs. NHE, pH 7); therefore, the holes cannot oxide OH^- ions to produce ·OH groups. Obvious decrease in the photodecomposition rate was observed upon addition of BQ and EDTA-2Na (which led to rate decreases of approximately 77 and 26%, respectively), suggesting that the $\cdot O_2^-$ and h^+ generated in the system were the crucial active species in the catalytic oxidation of RhB.

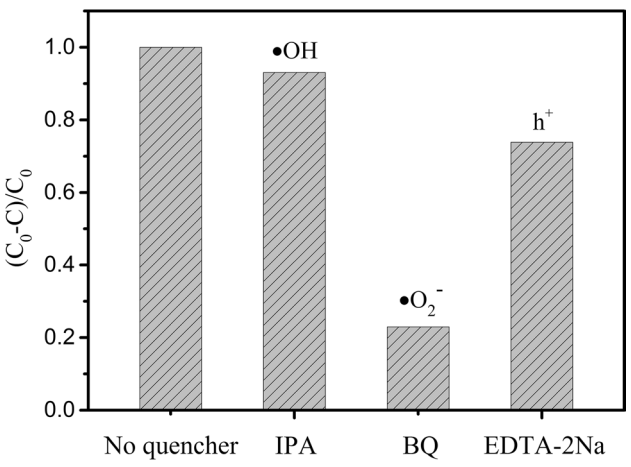

Fig. 8 Trapping experiments to identify the active species in the photodegradation of RhB over 0.1CN/BiOCl under visible light irradiation

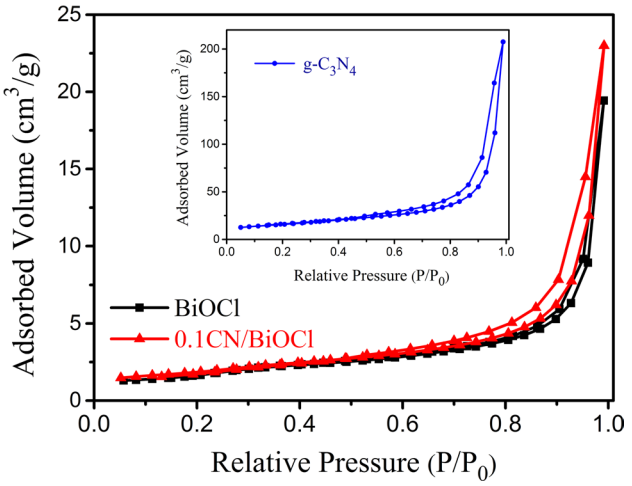

Fig. 9 N_2 adsorption–desorption isotherms of pure BiOCl, g-C_3N_4, and 0.1CN/BiOCl

Figure 9 shows the N_2 adsorption–desorption isotherms of pure BiOCl, g-C_3N_4, and 0.1CN/BiOCl. The curves allow determining the BET specific surface areas and pore sizes. The isotherms of all powders can be classified as type IV with H3 hysteresis loop, indicating the presence of mesoporous or narrow slits, which might have been formed by stacking of nanosheets. The BET specific surface areas of BiOCl, g-C_3N_4, and 0.1CN/BiOCl are 6.03, 55.44, and 6.60 m^2/g, respectively, whereas the corresponding average pore sizes are 19.95, 25.66, and 22.50 nm, respectively. The hybridization of g-C_3N_4 thus not only enhances the BET surface area of the catalysts, but also increases the pore sizes of the gaps generated between the nanosheets. It is well known that large BET specific surface areas offer more active sites for photocatalysis and also improve the capacity to adsorb degradation agents. The large size of narrow slit denotes a good dispersity of the compounds, which can enhance the absorption and transmission of the irradiated light. These results thus corroborate the conclusions of the SEM, DRS, and photodegradation analyses.

Based on the above analyses of PL and trapping experiments, the formation of *p–n* heterostructures at the interface and the possible charge transfer mechanism for the enhanced photocatalytic activity can be described as illustrated in Fig. 10. As the *p–n* g-C_3N_4/BiOCl heterojunction is formed, charge migration may contribute to the equilibration of the new Fermi levels in the composites. In addition, the porous structure contributed to extend the transmission distance of the illumination light and maximize the utilization of the photon energy. Following excitation of the g-C_3N_4 and RhB molecules under visible light illumination, the photoinduced electrons generated from the lowest unoccupied molecular orbital (LUMO) of RhB could inject into the CB of both g-C_3N_4 and BiOCl and the excited electrons

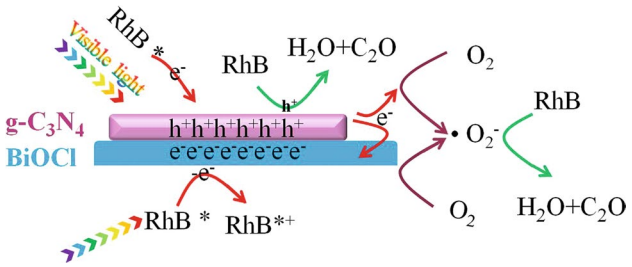

Fig. 10 Simplified schematic illustration of photocatalytic degradation of RhB over the *p–n* g-C_3N_4/BiOCl nanosheets under visible light irradiation

migrated from the VB of g-C_3N_4 to the CB of it also could transfer to the CB of BiOCl due to the more positive potential of BiOCl. Then the photoinduced electrons in the CB of g-C_3N_4 and BiOCl transferred to the surface of particles and were captured by the oxygen molecules adsorbed on the surface of the photocatalysts, producing ($\cdot O_2^-$) radicals to decompose RhB into H_2O and CO_2 or other small molecular products. At the same time, the remaining holes on the VB of g-C_3N_4 could directly oxidize the degradation agents. The photoinduced electron–hole pairs were then successfully separated. Consequently, the enhanced photocatalytic activity of these systems could be primarily attributed to the dominant effect of the staggered band structure of the composites which effectively hinders hole-electron recombination, and the photosensitization of RhB.

4 Conclusions

2D g-C_3N_4/BiOCl nanocomposites were successfully synthesized by a simple deposition–precipitation method assisted by a sonochemical treatment. A *p–n* heterostructure was formed at the interface between g-C_3N_4 and BiOCl nanosheets. The visible light response performance of the composite nanosheets was significantly extended than that of BiOCl, owing to the hybridization of g-C_3N_4. The photodegradation experiments and PL emission spectra highlighted the lower recombination rate and the efficient separation of photoinduced charges in the composites. The optimal photocatalyst composition was identified as 0.1CN/BiOCl, presumably as a result of the efficient heterojunction interfaces formed between the two components in this case, which contributed to the effective migration of the charge carriers. In conclusion, the 2D *p–n* type heterostructure of the composites was identified as the primary factor leading to the enhanced photocatalytic performances of the composites, whereas the sensitization effect of the RhB dyes played a minor role, and the influence of specific exposed facets of BiOCl was not significant.

Acknowledgements The research is sponsored by the Research Fund for the Doctoral Program of Higher Education of China (RFDP, No. 20110007110009) and Science Foundation of China University of Petroleum, Beijing.

References

1. A. Fujishima, K. Honda, Nature **238**, 37 (1972)
2. X. Bai, L. Wang, R. Zong, Y. Zhu, J. Phys. Chem. C **117**, 9952 (2013)
3. S.Q. Yan, C.G. Long, J. Mater. Sci. **27**, 12079 (2016)
4. C. Yang, G. Gao, Z. Guo, L. Song, J. Chi, S. Gan, Appl. Surf. Sci. **400**, 365 (2017)
5. Z. Ni, Y. Sun, Y. Zhang, F. Dong, Appl. Surf. Sci **365**, 314 (2016)
6. Y. Zhang, Y. Zhang, B. Fu, M. Hong, M. Xiang, Z. Liu, H. Liu, S. Liu, J. Mater. Sci. **26**, 3179 (2015)
7. D. Wang, J. Zhang, L. Guo, X. Dong, H. Shen, F. Fu, Mater. Res. Bull. **83**, 387 (2016)
8. X. Zhang, S. Yu, Y. Liu, Q. Zhang, Y. Zhou, Appl. Surf. Sci. **396**, 652 (2017)
9. Q. Xing, Z. Han, S. Zhao, J. Mater. Sci. **28**, 295 (2017)
10. K.T. Liu, J. Li, J.B. Xu, F.L. Xu, L. Wang, L. Bian, J. Mater. Sci. **28** 5609 (2017)
11. X. Meng, Z. Zhang, Appl. Surf. Sci. **392**, 169 (2017)
12. S. Devesa, M.P. Graça, L.C. Costa, Mater. Res. Bull. **78**, 128 (2016)
13. J. Li, J. Mater. Sci. **27**, 9798 (2016)
14. L. Song, Y. Pang, Y. Zheng, C. Chen, L. Ge, J. Alloys Compd. **710**, 375 (2017)
15. H. Ma, M. Zhao, Y. Fu, C. Ma, X. Dong, X. Zhang, J. Mater. Sci. **27**, 4598 (2016)
16. C. Liu, B. Chai, J. Mater. Sci. **26**, 2296 (2015)
17. N. Liang, J. Zai, M. Xu, Q. Zhu, X. Wei, X. Qian, J. Mater. Chem. **2**, 4208 (2014)
18. H. Cheng, B. Huang, Y. Liu, Z. Wang, X. Qin, X. Zhang, Y. Dai, Chem. Commun. **48**, 9729 (2012)
19. G. Liu, L. Wang, H.G. Yang, H.M. Cheng, G.Q. Lu, J. Mater. Chem. **20**, 831 (2010)
20. F. Duo, Y. Wang, X. Mao, X. Zhang, Y. Wang, C. Fan, Appl. Surf. Sci. **340**, 35 (2015)
21. G. Zhu, M. Hojamberdiev, K.I. Katsumata, N. Matsushita, K. Okada, P. Liu, J. Zhou, Y. Liu, Adv. Powder Technol. **25**, 1292 (2014)
22. C. Cao, L. Xiao, C. Chen, Q. Cao, Appl. Surf. Sci. **357**, 1171 (2015)
23. C. Tan, G. Zhu, M. Hojamberdiev, K. Okada, J. Liang, X. Luo, P. Liu, Y. Liu, Appl. Catal. B **152–153**, 425 (2014)
24. Y. Chen, G. Zhu, Y. Liu, J. Gao, C. Wang, R. Zhu, P. Liu, J. Mater. Sci. **28**, 2859 (2017)
25. S. Shi, M.A. Gondal, A.A. Al-Saadi, R. Fajgar, J. Kupcik, X. Chang, K. Shen, Q. Xu, Z.S. Seddigi, J. Colloid Interf. Sci. **416**, 212 (2014)
26. F. Chang, Y. Xie, J. Zhang, J. Chen, C. Li, J. Wang, J. Luo, B. Deng, X. Hu, RSC Adv. **4**, 28519 (2014)
27. Q. Li, X. Zhao, J. Yang, C.J. Jia, Z. Jin, W. Fan, Nanoscale **7**, 18971 (2015)
28. Y. Yang, F. Zhou, S. Zhan, Y. Liu, Y. Yin, J. Inorg. Organomet. Polym Mater. **26**, 91 (2016)
29. X. Lu, K. Xu, P. Chen, K. Jia, S. Liu, C. Wu, J. Mater. Chem. A **2**, 18924 (2014)
30. J. Jiang, K. Zhao, X. Xiao, L. Zhang, J. Am. Chem. Soc. **134**, 4473 (2012)
31. H. Cheng, B. Huang, P. Wang, Z. Wang, Z. Lou, J. Wang, X. Qin, X. Zhang, Y. Dai, Chem. Commun. **47**, 7054 (2011)
32. Z. Yang, J. Li, F. Cheng, Z. Chen, X. Dong, J. Alloys Compd. **634**, 215 (2015)
33. L. Armelao, G. Bottaro, C. Maccato, E. Tondello, Dalton Trans. **41**, 5480 (2012)
34. L. Ye, J. Liu, Z. Jiang, T. Peng, L. Zan, Appl. Catal. B **142–143**, 1 (2013)
35. S. Wang, C. Li, T. Wang, P. Zhang, A. Li, J. Gong, J. Mater. Chem. **2**, 2885 (2014)
36. Q. Xiang, J. Yu, M. Jaroniec, J. Phys. Chem. C **115**, 7355 (2011)
37. S. Yang, Y. Gong, J. Zhang, L. Zhan, L. Ma, Z. Fang, R. Vajtai, X. Wang, P.M. Ajayan, Adv. Mater. **25**, 2452 (2013)
38. G. Zhang, J. Zhang, M. Zhang, X. Wang, J. Mater. Chem. **22**, 8083 (2012)
39. J. Liu, T. Zhang, Z. Wang, G. Dawson, W. Chen, J. Mater. Chem. **21**, 14398 (2011)
40. D. Feng, Z. Zhou, M. Bo, Polym. Degrad. Stab. **50**, 65 (1995)
41. L.F. Chen, X.D. Zhang, H.W. Liang, M. Kong, Q.F. Guan, P. Chen, Z.Y. Wu, S.H. Yu, ACS Nano **6**, 7092 (2012)
42. C. Chang, L. Zhu, S. Wang, X. Chu, L. Yue, ACS Appl. Mater. Interfaces **6**, 5083 (2014)
43. Y. Sun, W. Zhang, T. Xiong, Z. Zhao, F. Dong, R. Wang, W.K. Ho, J. Colloid Interf. Sci. **418**, 317 (2014)